All-Optical Cryogenic Thermometry Based on Nitrogen-Vacancy Centers in Nanodiamonds

M. Fukami, C.G. Yale, P. Andrich, X. Liu, F.J. Heremans, P.F. Nealey, and D.D. Awschalom

All-optical cryogenic thermometry based on NV centers in nanodiamonds

M. Fukami[1], C. G. Yale[1,†], P. Andrich[1,‡], X. Liu[1], F. J. Heremans[1,2], P. F. Nealey[1,2], D. D. Awschalom[1,2,*]

1. *Pritzker School of Molecular Engineering, University of Chicago, Chicago, IL 60637*
2. *Center for Molecular Engineering and Materials Science Division, Argonne National Lab, Lemont, IL 60439*

†Present address: Sandia National Laboratories, Albuquerque, NM, 87185
‡Present address: University of Cambridge, Cavendish Laboratory, JJ Thomson Ave, Cambridge CB3 0HE
*Email: awsch@uchicago.edu

ABSTRACT

The nitrogen-vacancy (NV) center in diamond has been recognized as a high-sensitivity nanometer-scale metrology platform. Thermometry has been a recent focus, with attention largely confined to room temperature applications. Temperature sensing at low temperatures, however, remains challenging as the sensitivity decreases for many commonly used techniques, which rely on a temperature dependent frequency shift of NV center's spin resonance and its control with microwaves. Here we use an alternative approach that does not require microwaves, ratiometric all-optical thermometry, and demonstrate that it may be utilized to liquid nitrogen temperatures without deterioration of the sensitivity. The use of an array of nanodiamonds embedded within a portable polydimethylsiloxane (PDMS) sheet provides a versatile temperature sensing platform that can probe a wide variety of systems without the configurational restrictions needed for applying microwaves. With this device, we observe a temperature gradient over tens of microns in a ferromagnetic-insulator substrate (yttrium iron garnet, YIG) under local heating by a resistive heater. This thermometry technique provides a cryogenically compatible, microwave-free, minimally invasive approach capable of probing local temperatures with few restrictions on the substrate materials.

I.   INTRODUCTION

Local temperature variation plays a central role in many-body physics governed by hydrodynamic descriptions [1], in biomolecular science [2], as well as in thermal engineering of integrated circuits. Among the existing high-sensitivity nanometer-scale thermometers, nitrogen vacancy (NV) centers in nanodiamonds (NDs) have emerged as promising temperature-sensitive fluorescent probes. The negatively-charged NV-center (NV⁻) consists of a ground state spin triplet manifold with a zero-field splitting $\mathcal{D} \simeq 2.87$ GHz that sensitively responds to temperatures, where the shift can be measured by reading out the spin optically [2-6]. By virtue of diamond's high thermal conductivity and NV⁻ centers' long spin coherence time, ND-based thermometry has been demonstrated in a variety of systems, such as within a living cell at room temperature [2]. The temperature response of $\mathcal{D}$ is significantly smaller at low temperatures, however, which reduces sensitivity and hinders the conventional thermometry technique [7].

Ratiometric all-optical thermometry has been proposed as an alternative to the conventional microwave spin-resonance thermometry technique with compatible sensitivity at room temperature [8-14]. It also enables temperature sensing without the application of microwaves, which removes concerns of microwave heating. Interestingly, the temperature sensitivity of the all-optical thermometer is estimated to improve at lower temperatures (see Supplementary Material, Sec. A [15]), and indicates that this technique can offer a path forward towards ND-based cryogenic thermometry. The use of an array of NDs on a polydimethylsiloxane (PDMS) sheet [16] combined with all-optical thermometry completely removes configurational restrictions needed for microwave applications, offering a versatile device capable of probing a wide variety of solid-state systems over tens of microns with an adjustable spatial resolution on the order of a few microns. This makes all-optical thermometry suitable for probing and imaging a variety of condensed matter systems, and may have advantages over conventional NV-center thermometry techniques depending on the required thermal or spatial resolutions as well as the potential microwave response of the target system.

Here we extend the all-optical thermometry technique based on the NV⁻ centers in NDs from room temperature to liquid nitrogen temperatures, $85\text{ K} \leq T \leq 300\text{ K}$, and demonstrate its application on a ferromagnetic insulator (yttrium iron garnet, YIG) substrate. In particular, we focus on YIG as a platform to demonstrate our sensing approach both because the microwaves used to manipulate NV centers in conventional thermometry would impact the magnetic spins in the YIG [17-19], and the low temperature thermal response of YIG is of interest in the

study of the spin-Seebeck effect [20-25]. We initially demonstrate that a laser-pulse sequence to control the NV centers' charge states improves the sensitivity of the all-optical thermometer by approximately a factor of $\sqrt{3}$. Next, we systematically study the temperature dependence of the sensitivity, demonstrating that it improves at cryogenic temperatures. Finally, we apply this all-optical cryogenic thermometry technique at $T = 170$ K to measure the surface temperature profile of a YIG slab in contact with a resistive heater, with the array of NDs embedded on the surface of a flexible PDMS sheet. The observed temperature gradient over a range of tens of micrometers confirms the applicability of the technique on the YIG substrate, indicating that it provides a tool for studying local thermal properties of a wide variety of substrates over a broad range of temperatures.

II. DEMONSTRATION OF CRYOGENIC ALL-OPTICAL THERMOMETRY

We focus on the temperature (T) dependence of the NV- centers' zero phonon line (ZPL) amplitude ratio (A), which is defined as the ratio of the ZPL intensity with respect to an average photoluminescence (PL) intensity in a spectral range around the ZPL. The experiment was conducted on an array of NDs containing ensembles of NV- centers measured with a confocal microscope using a high numerical aperture objective (NA=0.9), as shown in Fig. 1(a). For all the experiments in this study, the power of the (532-nm and 594-nm) lasers was fixed at 200 µW to reduce the heating below 0.5 K due to the YIG absorption [23]. An array of NDs embedded into the flexible PDMS sheet was placed on the surface of a 3.05-µm-thick YIG film grown on a 500-µm-thick gadolinium gallium garnet (GGG) substrate (MTI Corp.). The diameter of the spot with NDs in the PDMS sheet was 1000 nm, which is defined by our microfabrication technique [16]. A Ti/Au (thickness: 8nm/200nm) resistive heater, for local heating, was patterned directly on the YIG film using a lithographic process and the bottom of the GGG substrate was affixed to a copper thermal sink within a flow cryostat. In the experiment, the base temperature of the sample was stabilized within ±0.3 K with PID control. Although the chamber thermocouple is positioned a few centimeters away from the sample, the temperature accuracy was confirmed to be ±0.5 K using a calibration thermocouple right next to the sample position. Both characterization (section II) and application (section III) of the thermometry were conducted on the same device with a YIG substrate for consistency.

Figure 1(b) shows a two-dimensional PL scan of an individual spot in the array of NDs under continuous 594-nm excitation, with a horizontal linecut through the maximum shown in Fig. 1(c). The 594-nm light does not excite the neutrally-charged NV-center (NV^0) [26,27], which improves the spectral contrast of the ZPL of NV- photoluminescence [9]. Each spot in the array contains tens of NDs, where each ND contains hundreds of NV centers (Adamas Technology, NV-ND-100 nm, 3 ppm NV density). Hence, there are approximately 3000 NV centers in each spot. Interestingly, when we applied pulsed laser sequences as shown in Fig. 1(d), the PL was enhanced by a factor of ≈ 3, which improves the sensitivity by a factor of $\approx \sqrt{3}$ (see Supplementary Material, Sec. B [15]). The enhancement is due to the increased NV- population under the pulsed laser sequence as compared to the continuous 594 nm illumination [28-30]. It has been reported that the illumination of a continuous wave 532 nm (594 nm) laser results in a 75% (10%) steady state NV- occupancy [28]. Since the charge state conversion rate is slower than 100 kHz under our laser powers [28,31], we can estimate that the average NV- population under the pump-probe sequence is between 75% and 10%. Assuming the charge initialization rates for both lasers are approximately equal, we estimate that the NV- population is at $\simeq 40\%$. This would lead to a $\simeq 4$ enhancement in signal, which is consistent with the experimental observation. In the following measurements, we send the PL to a spectrometer and gate a single-photon sensitive CCD camera in the spectrometer triggered by the pulse sequences. Every spectral measurement was followed by a background measurement taken off the ND and the background counts were subtracted. We note that the 2 µs period of the pulsed laser sequence is limited by the maximum gating speed (500 kHz) of the CCD camera.

Figure 2(a) shows the PL spectra $L(h\nu)$ in the range 85 K $\leq T \leq$ 300 K. Monotonic change in the spectra is observed except near $T \simeq 230$ K and $T \simeq 150$ K, which are due to the melting point and the glass transition point of the PDMS, respectively. Since the PL spectrum is normalized such that the integral PL spectral intensity is unity, these transitions suggest that there is a redistribution of the PL spectral intensity. These effects may be due to a change in strain inside the NDs on the PDMS sheet or a change in the wavelength-dependence of the index of reflection and the transmission efficiency, though we have not examined these scenarios in detail. We note that the presence of the PDMS sheet does not change the thermometry property of NV centers except PL count rates, which is verified by the measurements done on NDs without a PDMS sheet (see Supplementary Material, Sec. D [15]). In the following, we focus on the ZPL peak at $h\nu \simeq 1.94$ eV (637 nm) and the spectral range around the ZPL: from 605

nm to 660 nm, which we define as $\mathcal{R}$ [9]. As shown in the inset of Fig. 2(b), we fit the relative spectrum $L/\langle L \rangle_R$ by a sum of a squared-Lorentzian function and an exponential function:

$$L(h\nu)/\langle L \rangle_R = A\frac{1}{[w^2+(h\nu-h\nu_{ZPL})^2]^2}+B\exp\left[-\frac{h(\nu-\nu_{ZPL})}{k_B\Theta}\right],\qquad(1)$$

where k_B is the Boltzmann constant, h is the Plank constant, $\langle L \rangle_R$ is the average PL intensity in $\mathcal{R}$ and $\{A,B,\Theta,w,\nu_{ZPL}\}$ are fitting parameters [32]. A squared-Lorentzian function instead of a Lorentzian function is used for better fits at cryogenic temperatures [33].

Figure 2(b) shows the temperature evolution of the ZPL amplitude ratio A and the temperature response dA/dT of the amplitude ratio. The solid and dotted curves are derived from the two fits of the reduced Debye-Waller factor (DWF) and the ZPL linewidth shown in Figs. 2(c) and 2(d). In this work, the reduced DWF ($(DWF)_R$) is defined as the ratio of the ZPL counts, which corresponds to the area under the squared-Lorentzian fit, to the total PL counts in $\mathcal{R}$. We fit the temperature dependence of $(DWF)_R$ with a Gaussian function $(DWF)_R = \alpha\exp(-\gamma T^2)$, where α and γ are the fitting parameters with γ related to the electron-phonon coupling, S, and the Debye temperature, T_D, by a relation $\gamma = 2\pi^2 S/3T_D^2$ [8,34]. In this experiment, we obtained $\gamma = (218\text{ K})^{-2}$, which corresponds to $T_D/\sqrt{S} = 560$ K. Though the value of $T_D/\sqrt{S}$ is almost half of that reported in Ref. [8], the difference is associated with the different size and number of NDs as well as the different NV density used in this study, and our result is consistent with a measurement conducted on NDs without the PDMS sheet within 25%. The temperature dependence of the ZPL linewidth, w, was fit by a second-order polynomial $w = a+bT^2$. From these fits, we obtained the amplitude ratio (A) through the equation (see Supplementary Material, Sec. E [15])

$$A = \frac{2\alpha\exp(-\gamma T^2)\Delta R}{\pi(a+bT^2)},\qquad(2)$$

where ΔR is the size of the spectral range R. Importantly, the temperature response dA/dT increases at low temperatures, which leads to the sensitivity improvement. The temperature response is maximum at $T \simeq 150$ K, which coincidentally corresponds to the glass transition temperature of the PDMS, though does not appear to be related to it based on the measurements done without the PDMS sheet. We note that the enhancement of dA/dT is limited by the existence of the constant offset (a) in the linewidth $w = a+bT^2$, which is due to the spectral resolution of the spectrometer that accounts for $\simeq 50\%$ of the linewidth and an inhomogeneous broadening caused by crystal strain variations both between different NDs and within the individual commercial NDs used in this study. These limitations could be overcome by optimizing the spectral resolution and introducing engineered nanoparticles [35], leading to an enhanced temperature response at cryogenic temperatures.

To fully characterize the sensitivity $\eta = \sigma_A\sqrt{\Delta t}|dA/dT|^{-1}$, where Δt is the integration time, we studied the uncertainty σ_A as a function of temperature. At each temperature, PL spectrum measurements with $\Delta t = 2.5$ s were repeated one hundred times (Fig. 3(a)). We then calculate the standard deviation σ_A for each data set and show its temperature dependence in Fig. 3(b). To quantitatively compare the results at different temperatures, σ_A is rescaled by a factor $\sqrt{C_{ZPL}\Delta t}$, where C_{ZPL} is the ZPL count rate shown in the inset of Fig. 3(c). The black curve in the inset shows a one-parameter (a_1) fit of the ZPL count rate $C_{ZPL} = a_1(DWF)_R^{(T)}$, where $(DWF)_R^{(T)}$ is the curve we obtain in Fig. 2(c) assuming that the temperature dependence of C_{ZPL} is dominated by that of the reduced DWF. The dashed red curve shows the lower bound when the noise is coming only from photon shot noise, while the dotted blue curve shows the lower bound when the CCD camera's dark-current shot noise also contributes to the noise in the measurement. These two curves are obtained by applying two different models for the background ratio (y) in the function $g(y)$ [36], which is of order one, in the equation (see Supplementary Material, Sec. F [15])

$$\sigma_A = g(y)A/\sqrt{C_{ZPL}\Delta t}\qquad(3)$$

The experimental observation is well explained by the dotted curve, demonstrating that the standard deviation σ_A is dominated by the combination of the ZPL photon shot noise and the CCD's dark current shot noise. The remaining contribution to the noise is associated with the background photon counts from the YIG/GGG substrate or its surface, which can be measured without the PDMS sheet.

Combining the temperature dependencies of σ_A and $|dA/dT|$ as shown in Figs. 3(c) and 2(b), we plot the temperature evolution of the sensitivity in Fig. 3(d). The curve can be modeled by the combination of the equations (2) and (3) (see Supplementary Material, Sec. G [15]):

$$\eta = \frac{g(y)}{2T\left(\dfrac{b}{a+bT^2}+\gamma\right)\sqrt{C_{\text{tot}}(\text{DWF})|_{T=0}}}\exp\left(\frac{1}{2}\gamma T^2\right), \tag{4}$$

where C_{tot} is the total PL count rate [37-39]. Importantly, the sensitivity improves at cryogenic temperatures in contrast to other NV-based thermometry techniques [2-6]. We note that the sensitivity calculated in this study at $T = 300$ K does not reach the level of the sensitivity provided in the previous report on all-optical thermometry at room temperature [9]; however, taking into account detection efficiency differences, our result is found to be fully consistent with the one in Ref. [9]. In our experiment, the ZPL count rates were orders of magnitude smaller than those measured in the former study, where the ZPL counts rate from a single ND containing 100 NV centers was observed to be $C_{\text{ZPL},1}^{(295\text{ K})} = 900$ kcps at $T = 295$ K [9], in contrast to our measurement of $C_{\text{ZPL},2}^{(295\text{ K})} = 0.76$ kcps at $T = 295$ K. To compare our result with the previous study, we define a projected sensitivity [8] $\eta_{\text{proj}} = \sqrt{C_{\text{ZPL},2}^{(295\text{ K})}/C_{\text{ZPL},1}^{(295\text{ K})}}\,\eta$ and it is shown in the right axis of the Fig. 3(d). Though the projected sensitivity merely gives a rough estimate of a sensitivity given a higher detection efficiency of the PL, it also shows our result is consistent with the previous report [9]. To further improve the sensitivity at low temperatures, one could increase the ZPL count rate by improving the detection efficiency and utilizing brighter NDs that contain more NV$^-$ centers. For example, if we can improve the detection efficiency up to the level of that reported in Ref. [14], we would achieve $\times\sqrt{100}$ improvement in sensitivity under similar laser powers. While the total internal reflection inside the PDMS sheet reduces the detection efficiency by approximately a factor of three, it does not fully explain the detection efficiency differences. A more detailed analysis of the photon losses in our setup needs to be performed as some contributions are still not identified. Alternatively, using a larger diamond particle with 1 μm diameter and 10 ppm NV density [9], the sensitivity could be improved by a factor of $\simeq \sqrt{300}$, with a minor loss in spatial resolution. We note that we did not explore the effect below liquid nitrogen temperatures as equation (4) predicts that the sensitivity becomes monotonically worse.

III.   SURFACE TEMPERATURE IMAGING OF A YIG FILM

To demonstrate the applicability of the all-optical thermometer, we apply an 80-mA current to the resistive heater to generate a temperature gradient in the YIG and measure the spatial temperature variation of the YIG surface using an array of NDs, as illustrated in Fig. 1(a). Since the YIG has spin-wave resonances at microwave frequencies near $\mathcal{D}$ [17-19], this measurement confirms that the all-optical thermometry technique can be used independently of substrate materials where microwave control is problematic. The experiment is conducted at 170 K, which is above the glass transition temperature of the PDMS and the proximity of the NDs on the YIG surface is ensured. Figure 4(a) shows a two-dimensional spatial scan of the PL from the array of NDs used in this study. We use 25 spots in the array to construct the temperature profile, which are approximately evenly distributed and bright without spatial broadenings. Each of these 25 spots is calibrated individually to ensure the accuracy of the temperature measurements (see Supplemental Material, Sec. H [15]). Temperature dependencies of $\{B, \Theta, w, v_{\text{ZPL}}\}$ in addition to A are utilized for calculating the local temperature. For each measurement, the PL is collected in total for 500 s.

Figure 4(b) shows the resulting temperature profile of the YIG surface, where we observe a temperature decay on the order of tens-of-microns from the heat source. The temperature of each spot as a function of the distance from the heater is shown in Fig. 4(c). Note that the error accounts for both the inaccuracy due to the calibration and the sensitivity. The distribution of the errors is associated with the use of different sized nanoparticles along with the number of NDs per spot, which may be equalized by using a single diamond microparticle with standardized size after centrifugation. The data fits well to the Green's function to the 2D Poisson equation, showing that the temperature field in the YIG approximately follows the steady state diffusion equation

with a single heat carrier. We note that the Poisson equation is not accurate in YIG because there are two kinds of heat carriers, phonons and magnons. A deviation from the Poisson equation is expected near the heat source within a length scale of a magnon-phonon thermalization, which is much smaller than a few micrometers [22,23,25] (see Supplementary Material, Sec. I [15]). In our experiment, however, we do not observe a deviation from the Poisson equation as we are limited by the temperature resolution $\simeq 1$ K and the spatial resolution $\simeq 1$ μm. We also note that in the field of spin-caloritronics, lock-in infrared thermography techniques have recently been used to investigate thermo-spin or magneto-thermoelectric effects at room temperature [40-42]. The spatial and temperature resolutions of those methods are $\simeq 10$ μm and $\simeq 0.1$ mK, respectively. While the temperature sensitivity currently achievable with our method is not comparable to the ones used in the study of the emergent spin-caloritronics effects, such as the spin Peltier effect, the better spatial resolution may enable crucial investigation of the details of these systems in the future.

IV. CONCLUSION

We demonstrate and characterize an all-optical thermometry technique based on NV$^-$ center ensembles in ND that can be deployed from room temperature to liquid nitrogen temperatures, with a sensitivity that increases with decreasing temperature. Furthermore, the PL intensity of NV$^-$ centers is enhanced by implementing pulse sequences to convert NV^0 into NV$^-$, leading to a higher temperature sensitivity by approximately a factor of $\sqrt{3}$. Systematic noise analysis reveals that the sensitivity is limited by the shot noise and the inhomogeneous broadening of the ZPL linewidth, suggesting a pathway for further sensitivity improvements by optimizing the spectral resolution (see Supplementary Material, Sec. J [15]), improving the PL detection efficiency, and introducing engineered NDs with high brightness and homogeneous crystal strains. Taking advantage of an array of NDs embedded in a flexible PDMS sheet, we show the utility of the all-optical thermometer at $T = 170$ K by measuring the surface temperature profile of a YIG slab thermally driven by a resistive heater. This all-optical thermometry technique along with the versatility of the ND membrane array provides a microwave-free, minimally invasive, and cryogenically compatible way of measuring local temperatures within a variety of substrate materials.

References:
[1]   S. A. Hartnoll, P. K. Kovtun, M. Müller, and S. Sachdev, Theory of the Nernst effect near quantum phase transitions in condensed matter and in dyonic black holes, Phys. Rev. B **76**, 144502 (2007).
[2]   G. Kucsko, P. C. Maurer, N. Y. Yao, M. Kubo, H. J. Noh, P. K. Lo, H. Park, and M. D. Lukin, Nanometre-scale thermometry in a living cell, Nature **500**, 54 (2013).
[3]   V. M. Acosta, E. Bauch, M. P. Ledbetter, A. Waxman, L.-S. Bouchard, and D. Budker, Temperature Dependence of the Nitrogen-Vacancy Magnetic Resonance in Diamond, Phys. Rev. Lett. **104**, 070801 (2010)
[4]   P. Neumann, I. Jakobi, F. Dolde, C. Burk, R. Reuter, G. Waldherr, J. Honert, T. Wolf, A. Brunner, J. H. Shim, D. Suter, H. Sumiya, J. Isoya, and J. Wrachtrup, High-precision nanoscale temperature sensing using single defects in diamond, Nano Lett. **13**, 2738 (2013).
[5]   D. M. Toyli, C. F. de las Casas, D. J. Christle, V. V. Dobrovitski, and D. D. Awschalom, Fluorescence thermometry enhanced by the quantum coherence of single spins in diamond, Proc. Natl. Acad. Sci. **110**, 8417 (2013).
[6]   N. Wang, G. Liu, W. Leong, H. Zeng, X. Feng, S. Li, F. Dolde, H. Fedder, J. Wrachtrup, X. Cui, S. Yang, Q. Li, and R. Liu, Magnetic Criticality Enhanced Hybrid Nanodiamond Thermometer under Ambient Conditions. Phys. Rev. X **8**, 011042 (2018).
[7]   M. W. Doherty, V. M. Acosta, A. Jarmola, M. S. J. Barson, N. B. Manson, D. Budker, and L. C. L. Hollenberg, Temperature shifts of the resonances of the NV$^-$ center in diamond, Phys. Rev. B **90**, 041201(R) (2014).
[8]   T. Plakhotnik, M. W. Doherty, J. H. Cole, R. Chapman, and N. B. Manson, All-optical thermometry and thermal properties of the optically detected spin resonances of the NV$^-$ center in nanodiamond, Nano Lett. **14**, 4989 (2014).

[9]   T. Plakhotnik, H. Aman, and H. C. Chang, All-optical single-nanoparticle ratiometric thermometry with a noise floor of 0.3KHz−1/2, Nanotechnology **26**, 245501 (2015).

[10]   C. T. Nguyen, R. E. Evans, A. Sipahigil, M. K. Bhaskar, D. D. Sukachev, V. N. Agafonov, V. A. Davydov, L. F. Kulikova, F. Jelezko, and M. D. Lukin, All-optical nanoscale thermometry with silicon-vacancy centers in diamond, Appl. Phys. Lett. **112**, 203102 (2018).

[11]   M. Alkahtani, I. Cojocaru, X. Liu, T. Herzig, J. Meijer, J. Küpper, Tobias Lühmann, A. V. Akimov, and P. R. Hemmer, Tin-vacancy in diamonds for luminescent thermometry, Appl. Phys. Lett. **112**, 241902 (2018).

[12]   J.-W. Fan, I. Cojocaru, J. Becker, I. V. Fedotov, M. H. A. Alkahtani, A. Alajlan, S. Blakley, M. Rezaee, A. Lyamkina, Y. N. Palyanov, Y. M. Borzdov, Y.-P. Yang, A. Zheltikov, P. Hemmer, and A. V. Akimov, Germanium-vacancy color center in diamond as a temperature sensor, ACS Photonics **5**, 765 (2018).

[13]   T.T. Tran, B. Regan, E.A. Ekimov, Z. Mu, Z. Yu, W. Gao, P. Narang, A.S. Solntsev, M. Toth, I. Aharonovich, and C. Bradac, Anti-stokes excitation of solid-state quantum emitters for nanoscale thermometry, arXiv:1810.05265 (2018).

[14]   P.-C. Tsai, C. P. Epperla, J.-S. Huang, O. Y. Chen, C.-C. Wu, and H.-C. Chang, Measuring nanoscale thermostability of cell membranes with single gold–diamond nanohybrids, Angew. Chem., Int. Ed. **56**, 3025 (2017).

[15]   See Supplemental Material at [URL will be inserted by publisher] for details on the derivations, experimental setup, the optimization of the experimental condition, and the results without the PDMS film.

[16]   P. Andrich, J. Li, X. Liu, F. J. Heremans, P. F. Nealey, and D. Awschalom, Microscale-resolution thermal mapping using a flexible platform of patterned quantum sensors, Nano Lett. **18**, 4684 (2018).

[17]   C. S. Wolfe, V. P. Bhallamudi, H. L. Wang, C. H. Du, S. Manuilov, R. M. Teeling-Smith, A. J. Berger, R. Adur, F. Y. Yang, and P. C. Hammel, Off-resonant manipulation of spins in diamond via precessing magnetization of a proximal ferromagnet, Phys. Rev. B **89**, 180406(R) (2014).

[18]   P. Andrich, C. F. de las Casas, X. Liu, H. L. Bretscher, J. R. Berman, F. J. Heremans, P. F. Nealey, and D. D. Awschalom, Long-range spin wave mediated control of defect qubits in nanodiamonds, NPJ Quantum Inf. **3**, 28 (2017).

[19]   C. Du, T. van der Sar, T. X. Zhou, P. Upadhyaya, F. Casola, H. Zhang, M. C. Onbasli, C. A. Ross, R. L. Walsworth, Y. Tserkovnyak, and A. Yacoby, Control and local measurement of the spin chemical potential in a magnetic insulator, Science **357**, 195 (2017).

[20]   K. Uchida, S. Takahashi, K. Harii, J. Ieda, W. Koshibae, K. Ando, S. Maekawa, and E. Saitoh, Observation of the spin Seebeck effect, Nature (London) **455**, 778 (2008).

[21]   C. M. Jaworski, J. Yang, S. MacK, D. D. Awschalom, R. C. Myers, and J. P. Heremans, Spin-Seebeck effect: a phonon driven spin distribution, Phys. Rev. Lett. **106**, (2011).

[22]   M. Schreier, A. Kamra, M. Weiler, J. Xiao, G. E. W. Bauer, R. Gross, and S. T. B. Goennenwein, Magnon, phonon, and electron temperature profiles and the spin Seebeck effect in magnetic insulator/normal metal hybrid structures, Phys. Rev. B **88**, 094410 (2013).

[23]   K. An, K. S. Olsson, A. Weathers, S. Sullivan, X. Chen, X. Li, L. G. Marshall, X. Ma, N. Klimovich, J. Zhou, L. Shi, and X. Li, Magnons and phonons optically driven out of local equilibrium in a magnetic insulator, Phys. Rev. Lett. **117**, 107202 (2016).

[24]   B. L. Giles, Z. Yang, J. S. Jamison, J. M. Gomez-Perez, S. Vélez, L. E. Hueso, F. Casanova, and R. C. Myers, Thermally driven long-range magnon spin currents in yttrium iron garnet due to intrinsic spin Seebeck effect, Phys. Rev. B **96**, 180412(R) (2017).

[25]   A. Prakash, B. Flebus, J. Brangham, F. Yang, Y. Tserkovnyak, and J. P. Heremans, Evidence for the role of the magnon energy relaxation length in the spin Seebeck effect, Phys. Rev. B **97**, 020408(R) (2018).

[26]   A. Gali, Theory of the neutral nitrogen-vacancy center in diamond and its application to the realization of a qubit, Phys. Rev. B **79**, 235210 (2009).

[27]   S. Felton, A. M. Edmonds, and M. E. Newton, Electron paramagnetic resonance studies of the neutral nitrogen vacancy in diamond, Phys. Rev. B **77**, 081201(R) (2008).

[28]   N. Aslam, G. Waldherr, P. Neumann, F. Jelezko, and J. Wrachtrup, Photo-induced ionization dynamics of the nitrogen vacancy defect in diamond investigated by single-shot charge state detection, New J. Phys. **15**, 013064 (2013).

[29]   D. A. Hopper, R. R. Grote, S. M. Parks, and L. C. Bassett, Amplified sensitivity of nitrogen-vacancy spins in nanodiamonds using all-optical charge readout, ACS Nano **12**, 4678 (2018).

[30]   X. D. Chen, S. Li, A. Shen, Y. Dong, C. H. Dong, G. C. Guo, and F. W. Sun, Near-infrared-enhanced charge-state conversion for low-power optical nanoscopy with nitrogen-vacancy centers in diamond, Phys. Rev. Appl. **7**, 014008 (2017).

[31]   X. D. Chen, L. M. Zhou, C. L. Zou, C. C. Li, Y. Dong, F. W. Sun, and G. C. Guo, Spin depolarization effect induced by charge state conversion of nitrogen vacancy center in diamond, Phys. Rev. B **92**, 104301 (2015).

[32]   J. D. Dow and D. Redfield, Toward a unified theory of Urbach's rule and exponential absorption edges, Phys. Rev. B 5, 594 (1972).

[33]   G. Davies, The Jahn-Teller effect and vibronic coupling at deep levels in diamond, Rep. Prog. Phys. **44**, 787 (1981).

[34]   D. B. Fitchen, R. H. Silsbee, T. A. Fulton, and E. L. Wolf, Zero-phonon transitions of color centers in alkali halides, Phys. Rev. Lett. **11**, 275 (1963).

[35]   S. O. Hruszkewycz, W. Cha, P. Andrich, C. P. Anderson, A. Ulvestad, R. Harder, P. H. Fuoss, D. D. Awschalom, and F. J. Heremans, In situ study of annealing-induced strain relaxation in diamond nanoparticles using Bragg coherent diffraction imaging, APL Mater. **5**, 026105 (2017).

[36]   E. A. Donley and T. Plakhotnik, Statistics for single molecule spectroscopy data, Single Mol. **2**, 23 (2001).

[37]   A. T. Collins, M. F. Thomaz, M. I. B. Jorge, A. T. Collins, A. T. Collins, A. T. Collins, P. M. Spear, A. T. Collins, A. T. Collins, M. Stanley, A. T. Collins, S. C. Lawson, and J. Walker, Luminescence decay time of the 1.945 eV centre in type Ib diamond, J. Phys. C **16**, 2177 (1983).

[38]   T. Plakhotnik and D. Gruber, Phys. Luminescence of nitrogen-vacancy centers in nanodiamonds at temperatures between 300 and 700 K: perspectives on nanothermometry, Chem. Chem. Phys. **12**, 9751 (2010).

[39]   D. M. Toyli, D. J. Christle, A. Alkauskas, B. B. Buckley, C. G. Van de Walle, and D. D. Awschalom, Measurement and control of single nitrogen-vacancy center spins above 600 K, Phys. Rev. X **2**, 031001 (2012).

[40]   K. Uchida, S. Daimon, R. Iguchi, and E. Saitoh, Observation of anisotropic magneto-Peltier effect in nickel, Nature (London) **558**, 95 (2018).

[41]   J. Flipse, F. K. Dejene, D. Wagenaar, G. E. W. Bauer, J. Ben Youssef, and B. J. van Wees, Observation of the Spin Peltier Effect for Magnetic Insulators, Phys. Rev. Lett. **113**, 027601 (2014).

[42]   S. Daimon, R. Iguchi, T. Hioki, E. Saitoh, and K. Uchida, Thermal imaging of spin Peltier effect, Nature Communications **7**, 13754 (2016)
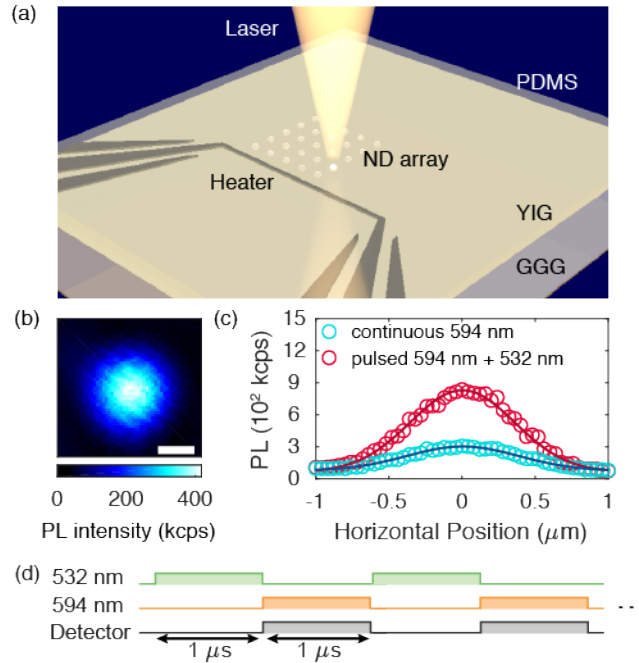
FIG. 1. (a) Schematic of an array of nanodiamonds (NDs) on a 3.05-μm-thick YIG film grown on a GGG substrate. NDs are embedded on the surface of a flexible PDMS sheet and the YIG film was patterned with a resistive heater (central wire has a width of 5 μm and a length of 200 μm). (b) Two-dimensional photoluminescence (PL) image of NV centers in NDs collected under continuous 594-nm excitation. The measurement was conducted at $T = 170$ K. Scale bar, 0.5 μm. (c) Line cuts of PL intensity profiles of NV centers under two different excitation pulse sequences. (d) Schematic of the pulse sequences of a 532-nm laser (NV⁻ charge state initialization), a 594-nm laser (NV⁻ detection) and a detector.
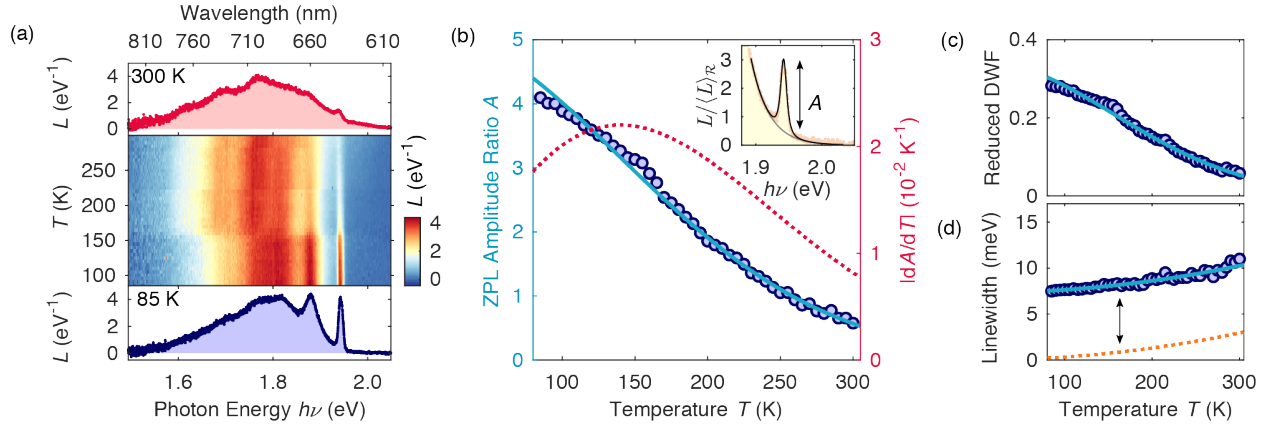
FIG. 2. (a) Evolution of NV centers' PL spectrum $L(h\nu)$ between 85 K and 300 K. The areas under the spectra are normalized to one. Discontinuities at $T \simeq 230$ K and $T \simeq 150$ K are associated with the PDMS's phase transitions. Top (bottom) graph shows the spectrum at 300 K (85 K). (b) Temperature dependence of the ZPL amplitude ratio A (left axis) and its temperature response $|dA/dT|$ (right axis). The solid blue curve and the dotted red curve are derived from the fits as shown in (c) and (d). Inset shows the fit of the ZPL spectrum at $T = 170$ K. (c) Reduced DWF as a function of T. A Gaussian-functional fit is shown. (d) ZPL linewidth as a function of T. The solid blue fit is the second-order polynomial $a + bT^2$ and the dotted orange curve shows bT^2.
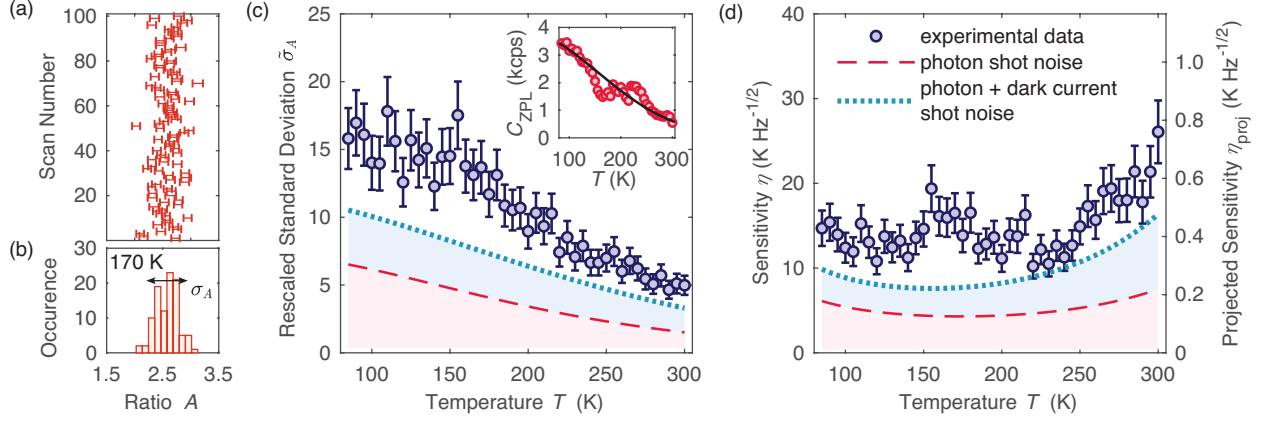
FIG. 3. (a) ZPL amplitude ratio scanned over 100 times at $T = 170$ K. A single scan consists of a PL integration time of $\Delta t = 2.5$ s. (b) Histogram built from the measurements in (a). The standard deviation σ_A is depicted. (c) Rescaled standard deviation $\tilde{\sigma}_A = \sigma_A \sqrt{C_{\mathrm{ZPL}} \Delta t}$ as a function of T, where C_{ZPL} is the ZPL counts rate. The dashed red curve and the dotted blue curve are lower bounds under two different models as defined in the main text. Inset shows C_{ZPL} as a function of T. Solid black curve shows a one-parameter (a_1) fit of the ZPL counts rate $C_{\mathrm{ZPL}}(T) = a_1 (\mathrm{DWF})_{\mathrm{R}}^{(T)}$, where $(\mathrm{DWF})_{\mathrm{R}}^{(T)}$ is the curve shown in Fig. 2 (c). (d) Temperature sensitivity η as a function of T. The dashed red and the dotted blue curves identify the lower bounds for the sensitivity. The spike near 160 K arises from the dip in the experimental data of C_{ZPL} as shown in the inset of (c). Right axis shows a projected sensitivity η_{proj} under the assumption of a higher detection rate of the PL as explained in the main text.
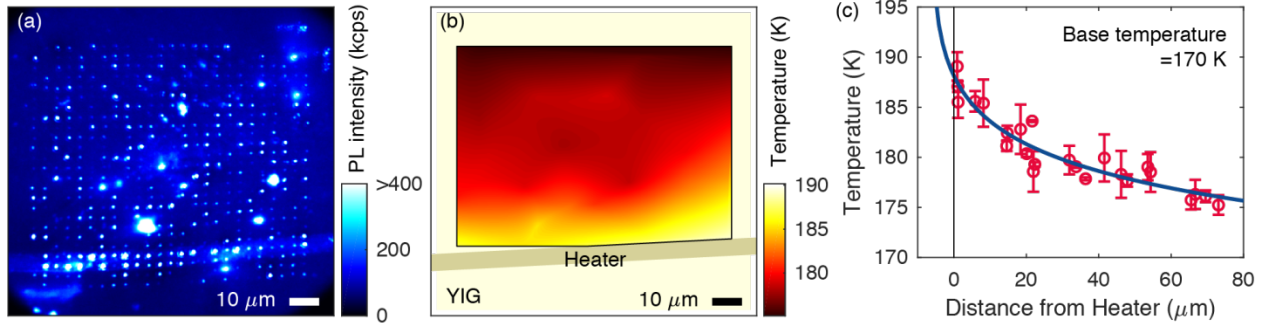
FIG. 4. (a) Spatial PL scan of NV centers in NDs in the array. (b) Two-dimensional temperature imaging of the YIG surface using NV centers in the array of NDs embedded on the surface of the PDMS sheet measured by the all-optical thermometry technique. An 80-mA current is applied to the resistive heater. The base temperature was set to $T = 170$ K. (c) YIG surface temperature as a function of the distance from the resistive heater. Fit with a logarithmic function is shown.